SAND2017-4871R

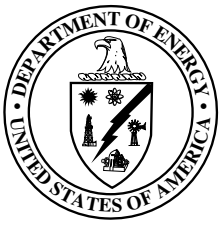

Sandia National Laboratories
Operated for the U.S. Department of Energy by
**National Technology and Engineering Solutions of Sandia, LLC**
Albuquerque, New Mexico 87185

*date:* May 5, 2017

*to:* Distribution

*from:* Judith A. Brown (1554) and Kevin N. Long (1554)

*subject:* Modeling the effect of glass microballoon (GMB) volume fraction on the behavior of Sylgard/GMB composites

## Executive Summary

This work was done to support customer questions about whether a Sylgard/Glass Microballoon (GMB) potting material in current use could be replaced with pure Sylgard and if this would significantly change stresses imparted to internal components under thermal cycling conditions. To address these questions, we provide micromechanics analysis of Sylgard/GMB materials using both analytic composite theory and finite element simulations to better understand the role of the GMB volume fraction in determining thermal expansion coefficient, elastic constants, and behavior in both confined and unconfined compression boundary value problems. A key finding is that damage accumulation in the material from breakage of GMBs significantly limits the global stress magnitude and results in a plateau stress behavior over large ranges of compressive strain. The magnitude of this plateau stress is reduced with higher volume fractions of GMBs. This effect is particularly pronounced in confined compression, which we estimate bears the most similarity to the application of interest. This stress-limiting damage mechanism is not present in pure Sylgard, however, and the result is much higher stresses under confined compression. Thus, we recommend that some volume fraction greater than 10% GMBs be used for confined deformation applications.

*Sandia National Laboratories is a multimission laboratory managed and operated by National Technology and Engineering Solutions of Sandia, LLC., a wholly owned subsidiary of Honeywell International, Inc., for the U.S. Department of Energy's National Nuclear Security Administration under contract DE-NA0003525.

# 1 Composite Theory Estimates of Elastic Constants and Thermal Expansion Coefficient for Sylgard® GMB

Analytic estimates of the bulk modulus, shear modulus, and coefficient of thermal expansion (CTE) for Sylgard®/GMB with different GMB volume fractions are pursued following the composite theory summarized in sections of [1]. This theory applies to two phase composites filled with spherical (isotropic elastic) inhomogeneities. Adapting this theory to the case of Sylgard® with GMBs requires elastic constants of a solid sphere that has the same structural response as a hollow glass microballoon at its outer boundary. Next, having estimates of the elastic constants of the Sylgard® 184 matrix phase and the effective GMB elastic constants, we compute properties of the composite Sylgard®/GMB as a function of volume fraction of GMBs. Details of these calculations are given in the previous memo SAND2016-2349 UUR [2] and only a brief summary of the theory is presented here.

It should be noted that this composite theory is only suitable in the dilute limit of the inhomogeneity phase and may not be accurate for high volume fractions of GMBs. Thus we present results up to volume fractions of 40% GMBs, but estimate that the results are most accurate below volume fractions of $\sim$20% GMBs.

From 3M's data sheets for A16/500 GMBs and from our previous analysis in [3], the mean balloon diameter is 60 microns and a typical balloon thickness is 1 micron. The 3M data sheets also specify the GMB wall material as "soda-lime-borosilicate glass". As the elastic constants of soda-lime and borosilicate glass are very similar, we use properties of borosilicate glass to represent the GMB material. The elastic constants of pure Sylgard 184 and the elastic constants of the GMB wall material used are presented in Table 1.

**Table 1.** Sylgard® 184 (100-10 PBW base resin to curing agent cured at 71 C) and Borosilicate Glass elastic constants

| **Property** | **Sylgard® 184** | **Borosilicate Glass** | **Solid Sphere Equivalent** |
|---|---|---|---|
| $K$ (MPa) | 920 [4] | 32,790* | 1,673* |
| $E$ (MPa) | 1.84 [4] | 61,000 [5][6] | – |
| $\mu$ (MPa) | 0.6135 [7] | 25,630* | 2,478* |
| $\nu$ | 0.4997 | 0.19 [5][6] | – |
| $\alpha(10^{-6}K^{-1})$ | 263 [4] | 3.3 [8] | 3.3 |

* Calculated quantity

### 1.1 Solid Sphere Equivalent Elastic Constants for The Mean Sized Glass Microballoon in 3M A16/500 GMBs

The first step is to determine the elastic constants of a solid sphere of material that is equivalent in mechanical behavior to the glass microballoons at their outer boundary. From the derivations given in [2], we determine the following expressions for bulk and shear modulii.

$$K_{\text{eff}} = \frac{4E_w t_0}{3D_0\,(1-\nu_w)}\,. \tag{1}$$

$$\mu_{\text{eff}} = \mu_w\,(1-f_0)\,. \tag{2}$$

The effective bulk modulus of the equivalent solid sphere has both structural ($t_0/D_0$) and material contributions ($E_w/(1-\nu_w)$), whereas the effective shear modulus depends only on the material properties of the solid wall ($\mu_w$) and the volume fraction of void space $f_0$.

Considering the mean diameter ($D_0$ = 60 microns) and typical shell thickness ($t_0$=1 micron) as well as properties for borosilicate glass (Table 1), we estimate the equivalent bulk modulus to be 1.67 GPa. For a thin shell of $t_0/D_0 = 1/60$, the volume fraction of void space is $f_0 \sim 0.9$. The shear modulus of the equivalent solid sphere is thus 2.48 GPa, which is $\sim$10% of the shear modulus of pure borosilicate glass. These equivalent solid sphere values are also shown in Table 1 for comparison with the matrix properties.

### 1.2 Composite Theory Estimates for Sylgard® GMB

The composite theory analysis in Section 2.3, Section 2.4 and Section 9.3 of [1] is then used to compute the composite properties for Sylgard®/GMB materials. We use the properties of pure Sylgard® 184 as the matrix material and the equivalent solid sphere properties as the inclusion material. The subscripts $m$ and $i$ refer to the matrix and inclusion phases respectively, and $f_i$ refers to the volume fraction of the inclusion phase (GMBs).

From Section 2.3 of [1], the composite bulk modulus is:

$$K_{\text{composite}} = K_m + \frac{f_i\,(K_i - K_m)}{1 + (1-f_i)\,[(K_i-K_m)/(K_m + 4\mu_m/3)]}\,. \tag{3}$$

The composite shear modulus is given by one of the solutions of the following quadratic equation as described in section 2.4 of [1]:

$$A\left(\frac{\mu}{\mu_m}\right)^2 + 2B\left(\frac{\mu}{\mu_m}\right) + C = 0\,. \tag{4}$$

The constants $A$, $B$, and $C$ are themselves functions of the matrix and inclusion properties and are described in detail in SAND2016-2349 UUR[2].

The composite coefficient of thermal expansion ($\alpha$) is derived by considering both thermal and stress boundary value problems imposed on a representative volume element containing both matrix and inclusion phases as described in Section 9.3 of [1]. For two-phase composites, the composite CTE can be computed from the CTEs and bulk moduli of the individual constituents and the composite bulk modulus:

$$\alpha_{\text{composite}} = \alpha_m + \frac{\alpha_i - \alpha_m}{1/K_i - 1/K_m}\left(\frac{1}{K_{\text{composite}}} - \frac{1}{K_m}\right). \tag{5}$$

We use the properties given in Table 1, and assume that the solid sphere equivalent CTE would be equal to that of pure borosilicate glass. The composite bulk modulus, $K_{\text{composite}}$ is computed from Eq. 3.

### 1.3 Composite Elastic Constants and CTE as a function of GMB Volume Fraction

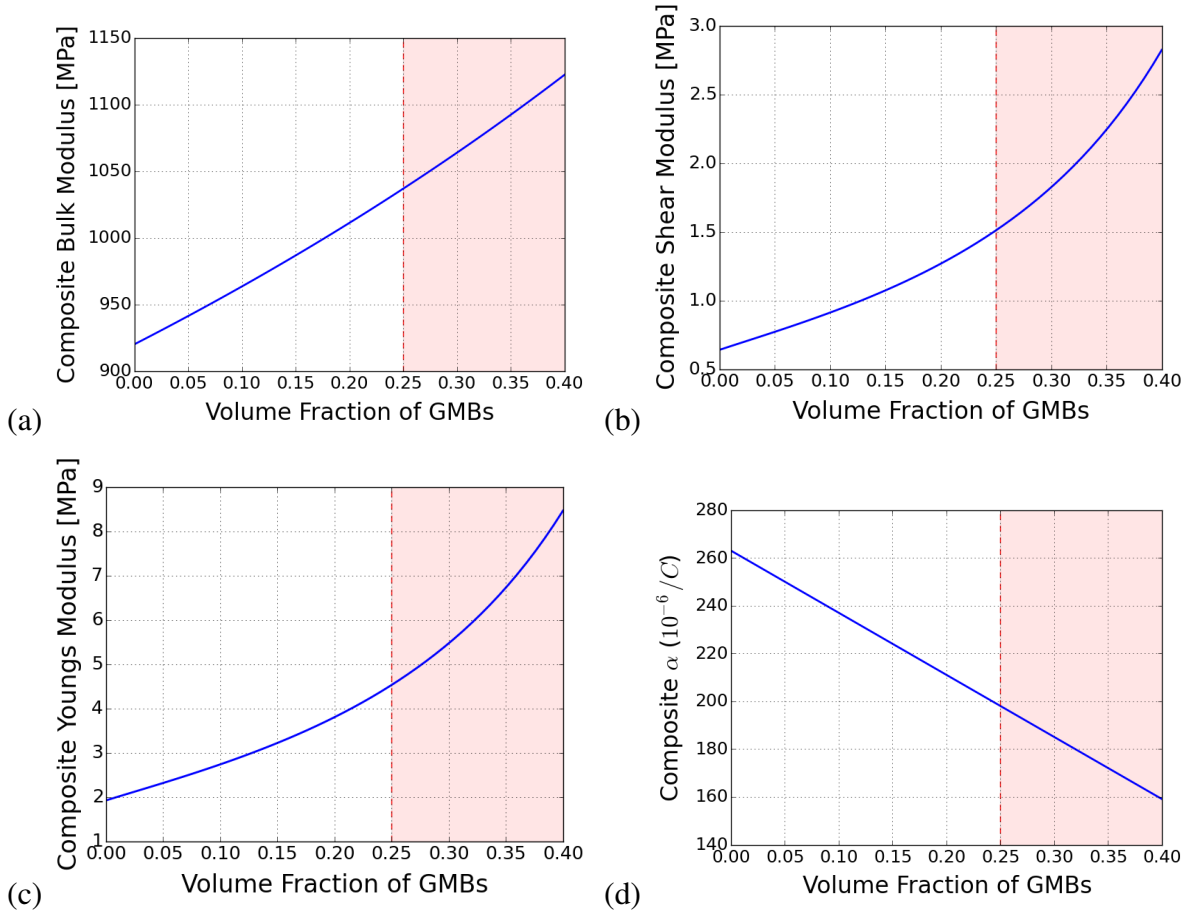


**Figure 1.** Elastic Constants (a-c) and thermal expansion coefficient (d) as a function of GMB volume fraction

The resulting elastic constants and CTE for composite Sylgard/GMB materials are shown in Figure 1 as a function of GMB volume fraction. The values of Young's modulus (Figure 1(c)) are calculated from the composite bulk and shear moduli assuming an isotropic material as:

$$E_{\text{composite}} = \frac{9K_{composite}\mu_{composite}}{3K_{composite} + \mu_{composite}}. \tag{6}$$

The shaded regions in Figure 1(a-d) represent volume fractions above which we estimate the "dilute limit" of the inclusion phase assumption may be violated and cause results at these volume fractions to be less accurate. Each of the elastic constants is predicted to increase with increasing GMB volume fraction, due to the higher elastic constants of the GMBs when compared to the matrix material. Comparisons of the elastic properties to experimental data at 0.37% volume fraction GMBs are found in previous studies [2], and it was concluded that this method provides a reasonable estimate of the bulk and shear moduli when considering uncertainty in the experimental values, and the limits of this composite theory at high GMB volume fractions. Our intuition suggests that while the initial bulk modulus should increase at low GMB volume fractions due to the higher GMB stiffness, it may not increase monotonically at large volume fractions due to effects not included in this composite theory, such as interaction between GMBs.

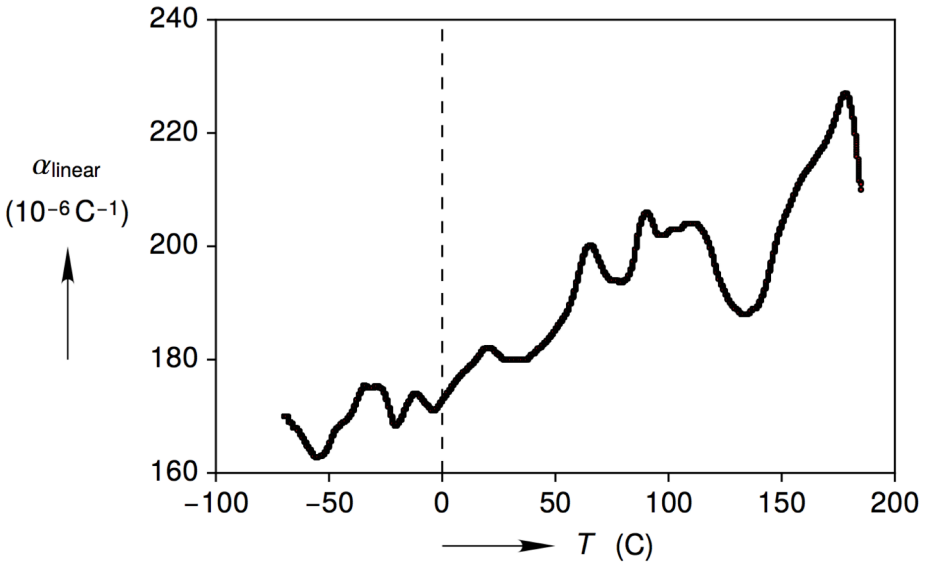


**Figure 2.** Thermal expansion coefficient vs. temperature for Sylgard®/GMB from [4]. Note that the legacy material formulation was used rather than the current formulation.

Conversely, the CTE of the composite decreases with increasing GMB volume fraction as the CTE of pure borosilicate glass is an order of magnitude smaller than that of pure Sylgard. For completeness, we supply the thermal expansion behavior vs. temperature of the Sylgard® GMB composite with 37% volume fill A16/500 GMBs from [4] in Figure 2. Comparing the composite theory calculation in Figure 1(d) at 0.37% GMB volume fraction with the data presented in Figure 2 at ∼25 C, it is seen that the experimental value ∼185 C is roughly 20 C higher than the calculated value of ∼162 C. Consequently, we conclude that the composite theory predictions of thermal expansion coefficient provide a reasonable estimate at room temperature, but perhaps most importantly identify the correct trend of this property vs. GMB volume fraction.

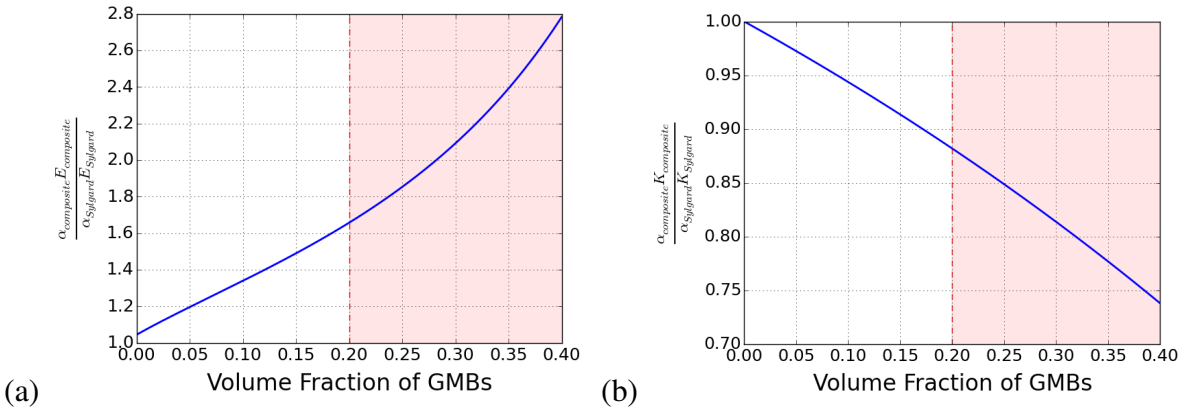


**Figure 3.** Ratios of the Sylgard/GMB composites with different GMB volume fractions to pure Sylgard for (a) Product of thermal expansion coefficient ($\alpha$) and Young's Modulus (E), (b) Product of thermal expansion coefficient ($\alpha$) and bulk modulus (K).

Finally, we show the product of coefficient of thermal expansion ($\alpha$) with Young's modulus in Figure 3(a) and bulk modulus in Figure 3(b). Since thermal stress is calculated as the product $E\alpha\Delta T$ under uniaxial deformation (unconfined conditions) and $K(3\alpha)\Delta T$ in volumetric deformation (confined conditions), this presents an idea of what thermal stresses would be produced over a fixed temperature change for materials with different GMB volume fractions compared with pure Sylgard. We show these quantities as ratios of the composite value compared to the value for pure Sylgard. From Figure 3(a), it can be seen that even though the composite CTE is reduced, at higher GMB volume fractions the increased composite stiffness is the dominating effect in the product $E\alpha$. Conversely, the addition of any volume fraction of GMBs acts to decrease the product $K\alpha$. Based on this, we can estimate that comparing Sylgard/GMB materials with pure Sylgard, thermal stresses in unconfined conditions may be amplified by the addition of GMBs due to increased Young's modulus, but in confined conditions, the thermal stresses may actually be reduced.

## 2 Finite Element Micromechanics Simulations

We next present results of Finite Element micromechanics simulations performed to better understand the role of GMB volume fraction on damage mechanisms in Sylgard/GMB composites. These models explicitly resolve the material meso-structure and allow us to study how damage evolution and local GMB interactions contribute to the global material response under large compressive strains. Two different boundary value problems of confined and unconfined compression are studied to provide insight into material behavior under different stress states.

### 2.1 Microstructure and Mesh Generation

A unique microstructure geometry with randomized GMB locations within a cube-shaped stochastic volume element (SVE) was created for each different GMB volume fraction. A fixed number of 40 GMBs was used in each SVE model, and the total SVE volume was calculated by considering

the number of GMBs and the volume fraction of the SVE that should be occupied by GMBs. This is then used to determine the length of each side of the SVE cube.

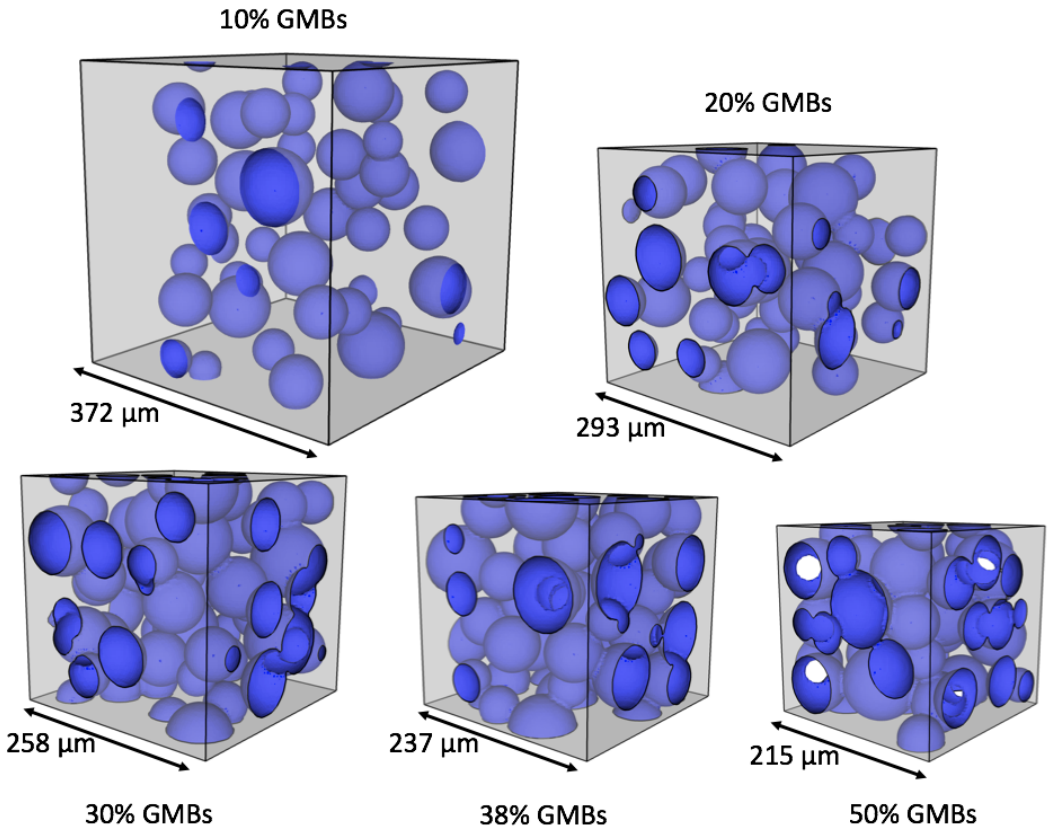


**Figure 4.** Microstructure models used for each different volume fraction of GMBs.

In each case, a Gaussian distribution of GMB sizes was used with a mean radius of 30 microns and standard deviation of 5 microns. The GMBs are allowed to intersect the faces of the cube, but not the edges or corners due to meshing constraints. GMBs are also allowed to intersect each other in order to achieve the desired volume fractions. Without allowing GMBs to intersect, generating the higher volume fractions of 38% and 50% is not feasible via this method. The SVE microstructures generated for each volume fraction are shown in Figure 4.

The SVE geometry is meshed using the Cubit Meshing and Geometry Toolkit developed at Sandia National Laboratories. The Sculpt meshing feature [9], which is part of the Cubit toolkit, is used to generate an all-hex mesh of the irregular Sylgard/GMB microstructure without requiring any geometry decomposition. The entire SVE structure is first meshed with HEX8 elements using the Sculpt tool, including the matrix structure and solid sphere placeholders at the location of each GMB. The solid elements filling each GMB placeholder structure are then deleted, and replaced with a layer of SHELL4 elements at each GMB-matrix interface. The result is the porous matrix structure meshed with solid hex elements, a layer of shell elements representing each hollow GMB, and a void region with no elements inside each GMB structure. This is illustrated in Figure 5.

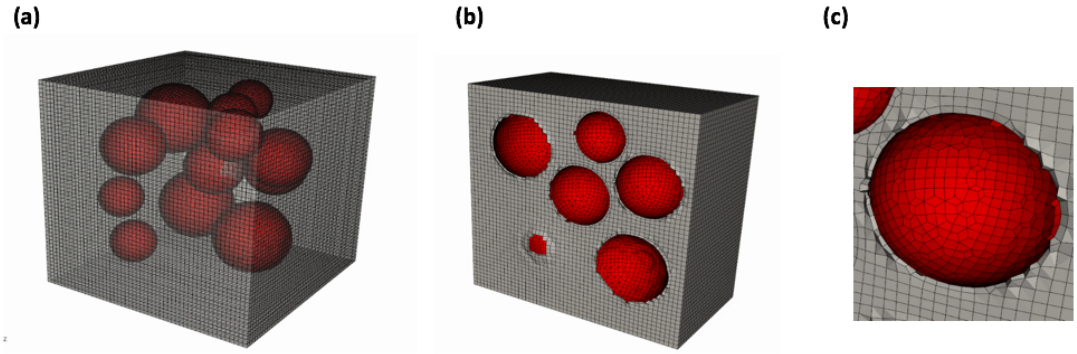


**Figure 5.** Example FE model meshed with Sculpt. (a) Entire mesh, (b) Entire mesh cross section, (c) Close-up cross section of single GMB-matrix interface. Solid matrix elements shown in grey, GMB shell elements shown in red.

We note that the matrix elements around the GMBs may appear slightly distorted in the cross-sectional images, but this is an artifact of the image rendering in Cubit rather than actual faceting of the mesh. Additionally, each GMB shell element is required to share all nodes with the adjacent matrix element. This ensures that the shell element will never separate from its neighbor matrix element, and forces the GMB shell elements to move concurrently with the matrix. This represents a perfectly bonded state between the matrix and GMBs. While debonding mechanisms may also be present during deformation, they are not considered in this analysis.

### 2.2 Material Models Used for Sylard 184 and Borosilicate Glass

Material parameterizations for Sylgard 184 (90-10) and borosilicate glass are presented here. An isotropic, linear viscoelastic representation for Sylgard 184 adopted from reference [10] is used with the Sierra/SM Universal Polymer Model. More details on this material model are available in [11]. We assume that the macroscale elastic properties of borosilicate glass apply to the GMBs, since we do not have mechanical property measurements at the sub-micron length scale (the characteristic thickness of a GMB). Isotropic elastic constants for borosilicate glass are taken from [5][6], and are the same as used in Section 1.2.

For all simulations, the GMBs are modeled using the Sierra/SM Multilinear Elastic-Plastic Hardening Model with Failure, which is modified to approximate a brittle failure mechanism. This is done by using a linear hardening function with slope equal to the elastic modulus and by setting the critical tearing parameter equal to zero, such that element failure begins immediately after the element reaches the yield stress and finishes when the critical crack opening (equivalent plastic) strain is reached. Balloon breakage is accomplished through death of the shell integration points and ultimately element death when all integration points fail in a shell. The failure is spread out over a 2% equivalent plastic strain to reduce the sensitivity of the microstructure to sudden changes in element behavior. This critical crack opening strain is used for model purposes and should not be interpreted here as physical without additional investigation in the literature.

We do not have a clear picture of how borosilicate glass fails at this length scale in reality because the fracture behavior of brittle materials is determined by the distribution of inherent flaws. Since we are working with shells of thickness order 1 micron, we expect inherent flaws to be small and the effective fracture strength of the material to be large. Therefore, to qualitatively observe failure of the GMBs in this microstructure, we estimated the yield stress to be 610 MPa, which is 1% of the Young's modulus for borosilicate glass.

The GMB material model input for Sierra/SM is shown here:

```
###------------------------------------------------------------------------------
###material model MLEP-fail set-up to simulate elastic fracture in shells
###Set criticical tearing parameter = 0 to cause failure as soon
###as stress > "yield stress"
    begin property specification for material GMBfail
        DENSITY           = {2520*1e6*1E-18}    # kg/m^3
        begin parameters for model ML_EP_FAIL
           shear modulus = 25.63E9       #Pa = pN/micron^2
           Youngs modulus = 61.0E9     #Pa
           beta = 1.0
           yield stress = {0.01*61.0E9}          #Pa     #1e2
           hardening function = MLEPhardening
           critical tearing parameter = 0
           critical crack opening strain = 2.0e-2   #estimated
           failure exponent = 1.0
        end parameters for model ML_EP_FAIL
   end property specification for material GMBfail
###------------------------------------------------------------------------------
 #this is made up such that slope of "hardening curve" is equal to Youngs modulus
  begin definition for function MLEPhardening
     type is piecewise linear
     abscissa is eqps
     begin values
        0.0 0.0
        0.5 30.5e9   #Pa
     end values
  end definition for function MLEPhardening
###------------------------------------------------------------------------------
```

### 2.3 Finite Element Simulations

Since we estimate the stress state in the application of interest to be a complex function of both material behavior and structure geometry, we model the finite deformation response of each SVE in Figure 4 in two boundary value problems (BVP) designed to represent confined and unconfined compression. This allows us to explore the effect of GMB volume fraction under global states of

uniaxial stress (unconfined compression) and uniaxial strain (confined compression). Both BVPs simulate applied compression to some prescribed strain value, followed by unloading back to zero strain. This is done through an applied displacement condition on the +X face of the model. Applied strain is related to applied displacement as as the nodal displacements applied to this face divided by the original length of the model (L0). All displacements are applied at a fixed strain rate of 0.15 $s^{-1}$.

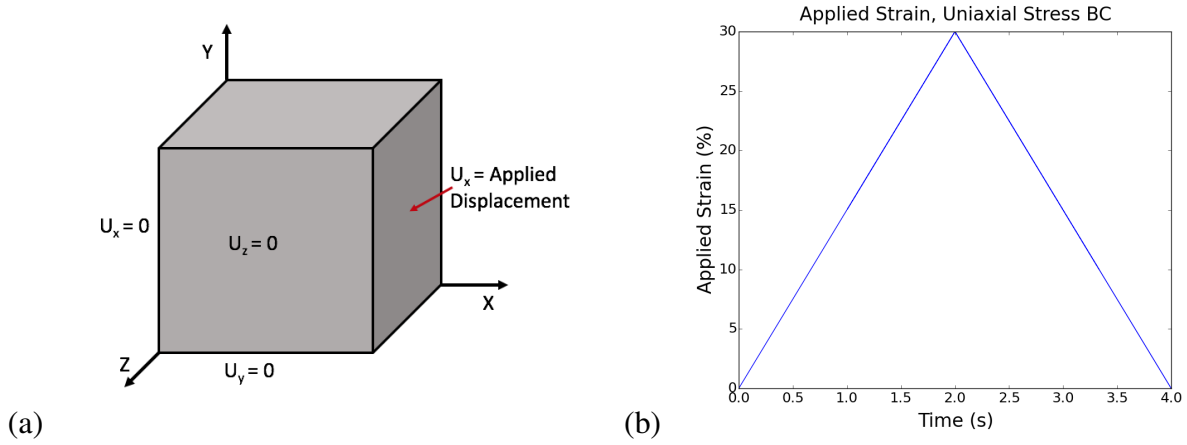


(a) (b)

**Figure 6.** Boundary conditions (a) and applied strain vs. time (b) for the unaixial stress boundary value problem.

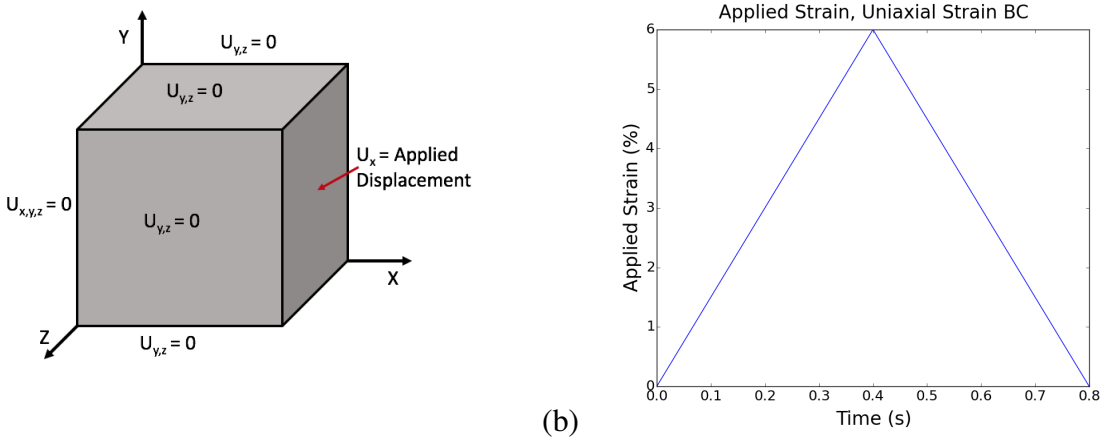


(a) (b)

**Figure 7.** Boundary conditions (a) and applied strain vs. time (b) for the unaixial strain boundary value problem.

Boundary conditions applied for the uniaxial stress case are shown in Figure 6. This BVP assumes 1/8 symmetry conditions and compresses the material to a maximum nominal strain of 30%. The boundary conditions applied for the uniaxial strain case are shown in Figure 7. For this BVP, all faces were constrained to only allow motion in the X-direction. The uniaxial strain case proved to be much less computationally robust, and thus we only compress this case to 6% nominal strain.

A short summary of other details and assumptions for these finite element simulations is listed here.

- Only compression BVPs were considered. While shear and tensile loading may be of interest, we focused on compression as the exemplar loading BVP for potted components.
- The simulations were performed using the Explicit Quasistatic Mode capability in Sierra/Solid Mechanics [12]. This method is used to provide a robust computational platform that can model complex mechanisms with which implicit solvers often have difficulty, including large localized deformations and pervasive contact. All cases were run using an explicit quasi-static mode time step size of $\sim 2$ x $10^{-6}$ s. We have performed some preliminary convergence studies on the quasi-static mode time step size necessary to achieve a reasonable approximation of quasi-static conditions using this method, with details available in [3].
- Any matrix elements that invert during the simulation are killed using element death. This was necessary to accommodate failure of multiple GMBs in a single simulation, as the matrix elements neighboring failed GMBs sometimes invert due to rapidly changing local stress states. We feel this doesn't have a large effect on global material behavior, however, as the percentage of matrix elements killed was less than 0.1% of the total matrix volume in all simulations.
- Self-contact was specified for the Sylgard matrix material to prevent artificial overlap of the matrix ligaments as the GMBs fail. We do not include contact between the GMB shell elements, with the assumption that artificial overlap of $1\mu$m wall thickness of the GMBs will be negligible compared to matrix deformation. Frictionless contact was used since a reasonable estimate of friction coefficient between matrix ligaments is currently unknown.
- The nominal stress-strain response was calculated using the nodal displacements and reaction forces on the +X of the model where the displacement boundary condition was applied. Nominal stress was calculated as the average reaction force at these nodes (F) divided by the original cross-sectional area in the x-z plane (A0), and nominal strain is calculated from the applied displacements as discussed above.
- The nominal stress-strain curves computed from the raw data were very noisy. We believe this is an artifact of the explicit quasi-static mode numerical methods used and as of yet have not determined its exact cause. However, the fundamental shape of the stress-strain curves reflects the expected behavior of Sylgard/GMB materials, and we believe that for the qualitative evaluation of deformation mechanisms that we attempt here, this noise effect can be ignored.

### 2.4 Predictions of Behavior in Uniaxial Stress Boundary Value Problem (Unconfined)

Figure 8(a) shows the nominal stress-strain response of Sylgard/GMB materials with various GMB volume fractions in the uniaxial stress BVP. The response of pure Sylgard (dark blue line) is also included for comparison. The cumulative percentage of dead shell elements for each Sylgard/GMB material is shown in Figure 8(b) as a metric to compare damage accumulation between materials. Additional metrics of the behavior, such as slopes of the initial load and unloading regions, plateau stress, and strain at the initial GMB breakage are shown in Table 2.4.

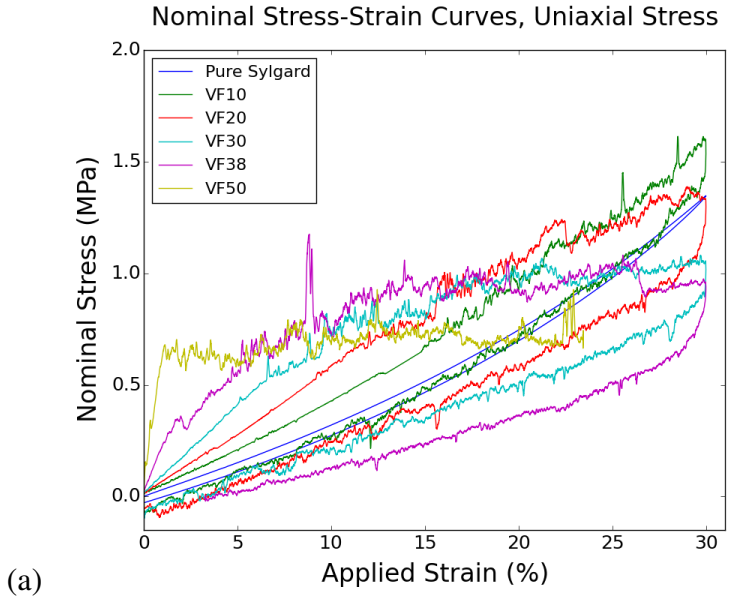


(a)

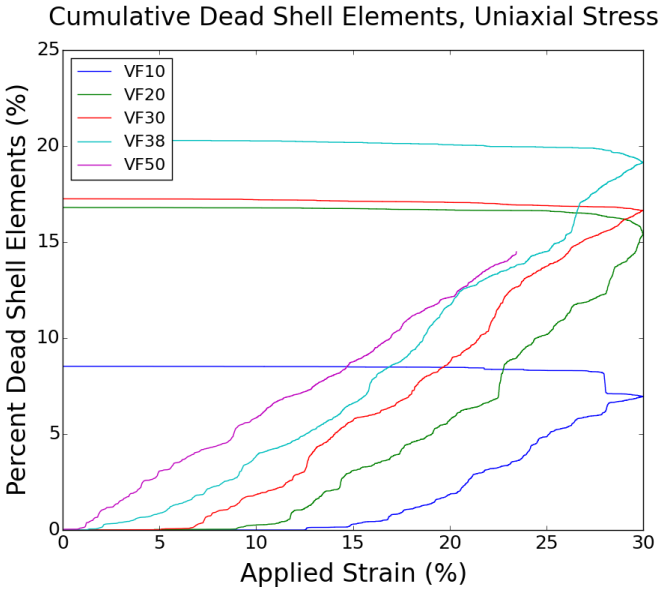


(b)

**Figure 8.** Stress-strain curves (a) and accumulated number of dead shell elements (b) for Sylgard/GMB materials with various volume fractions under the unaixial stress BVP.

**Table 2.** Summary of Load/Unload Slopes, Plateau Stress Behavior, and Strain at Initial GMB Breakage for various GMB volume fractions under uniaxial stress BVP (unconfined).

| **GMB Volume Fraction** | **Initial Loading Slope (MPa)** | **Unload Slope (MPa)** | **Plateau Stress (MPa)** | **Strain at Initial GMB Breakage** |
|---|---|---|---|---|
| Pure Sylgard | 3.21 | 3.24 | – | N/A |
| 10% | 7.21 | 5.1 | – | 12.49% |
| 20% | 8.92 | 3.3 | – | 4.65% |
| 30% | 11.25 | 3.0 | ∼1.0 | 2.66% |
| 38% | 25.53 | 2.5 | ∼0.9 | 1.23% |
| 50% | 69.15 | ** | ∼0.65 | 2.5e-7% |

** Simulation failed before unload, – No plateau behavior observed

With increasing GMB volume fraction, the initial loading slope becomes steeper indicating an initially stiffer material response. However, the GMBs also begin breaking sooner at higher GMB volume fractions, as shown by the lower strains at which dead shell elements begin to accumulate. This leads to the development of plateau stress behavior as the GMB breakage limits the maximum stress that can accumulate in the material. By contrast, the pure Sylgard material has the lowest loading slope but cannot exhibit any plateau behavior as this damage mechanism is not present in the pure material.

For this uniaxial stress boundary value problem, there appears to be a "critical volume fraction" above which plateau stress behavior is observed. The materials with 10% and 20% GMB volume fraction don't have any flattened plateau region, but rather, stress continues to increase fairly linearly even after GMBs have started to break. For the 30% and 38% GMB volume fraction materials, a hybrid/transition type behavior is observed where the stress-strain curve slowly flattens out and remains at fairly constant stress at high strains. The 50% GMB volume fraction material shows a flat plateau stress region at much lower strains, as GMBs begin breaking in this material almost immediately after it is loaded. It should be noted that the quantitative volume fraction at which the transition to plateau behavior occurs is highly dependent on the GMB failure criterion specified. Since our failure criterion was purely estimated, the behavior discussed above should be considered qualitatively representative but not quantitatively rigorous enough to identify the exact volume fraction required to produce plateau behavior.

Finally, the unload slopes of all the materials are similar to or lower than pure Sylgard, indicating that all materials have sustained some damage, and the GMBs do not contribute much to the material stiffness during the unload phase. Moreover, damaged Sylgard/GMB is more compliant than pure Sylgard. Also, very little additional damage is accumulated during the unloading, as seen by the flat regions of the accumulated dead shell elements with unloading strain in Figure 8(b).

Figures 9, 10, and 11 show snapshots of the modeled microstructures correlated with the individual stress-strain response and damage evolution for GMB volume fractions of 10%, 30%, and 50%, respectively. The differences in damage accumulation and plateau stress development can be clearly seen. For 10% GMB volume fraction, only one GMB shows damage at 15% strain, and only a few GMBs are broken even at 30% strain (Figure 9). This corresponds to a lack of clear plateau behavior in the stress strain curve for this low volume fraction. The 30% GMB volume fraction material shows roughly half of the GMBs are damaged at 15% strain, and most of them are damaged at 30% strain (Figure 10). The 50% GMB volume fraction material begins damaging GMBs at very small strains, and almost all the GMBs are damaged by 15% strain (Figure 11). This model failed to run to the full 30% strain, so the final microstructure snapshot is shown at the maximum strain achieved of ∼23%.

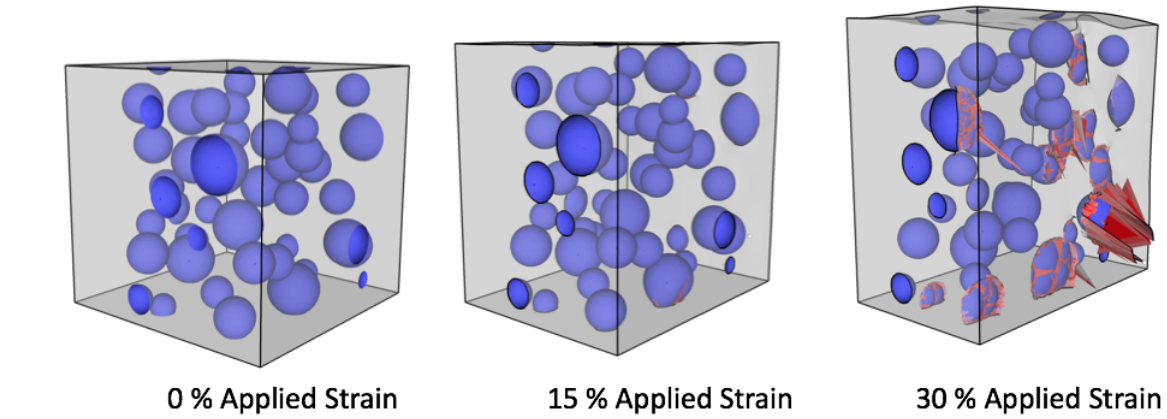


(a)

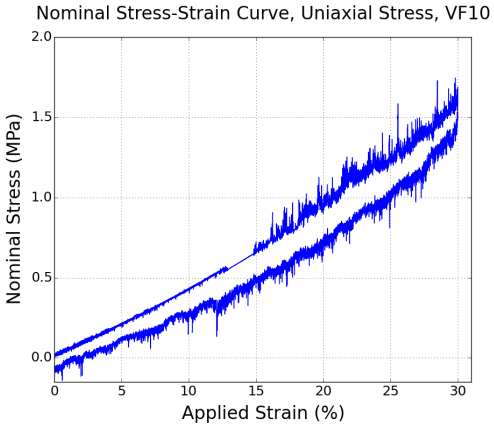


(b)

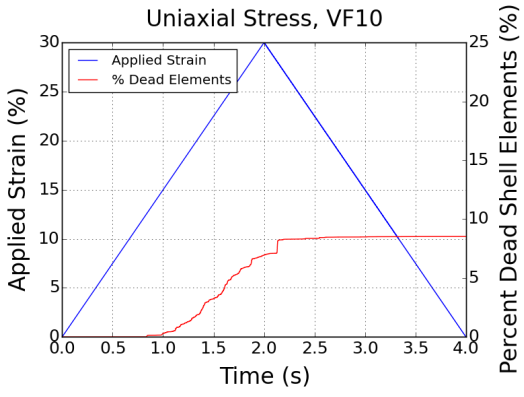


(c)

**Figure 9.** Sylgard/GMB with 10% volume fraction GMBs under unaixial stress BVP: (a) Deformation sequence with dead shell elements shown in red, (b) Nominal stress-strain curve, (c) Accumulated number of dead shell elements vs. time.

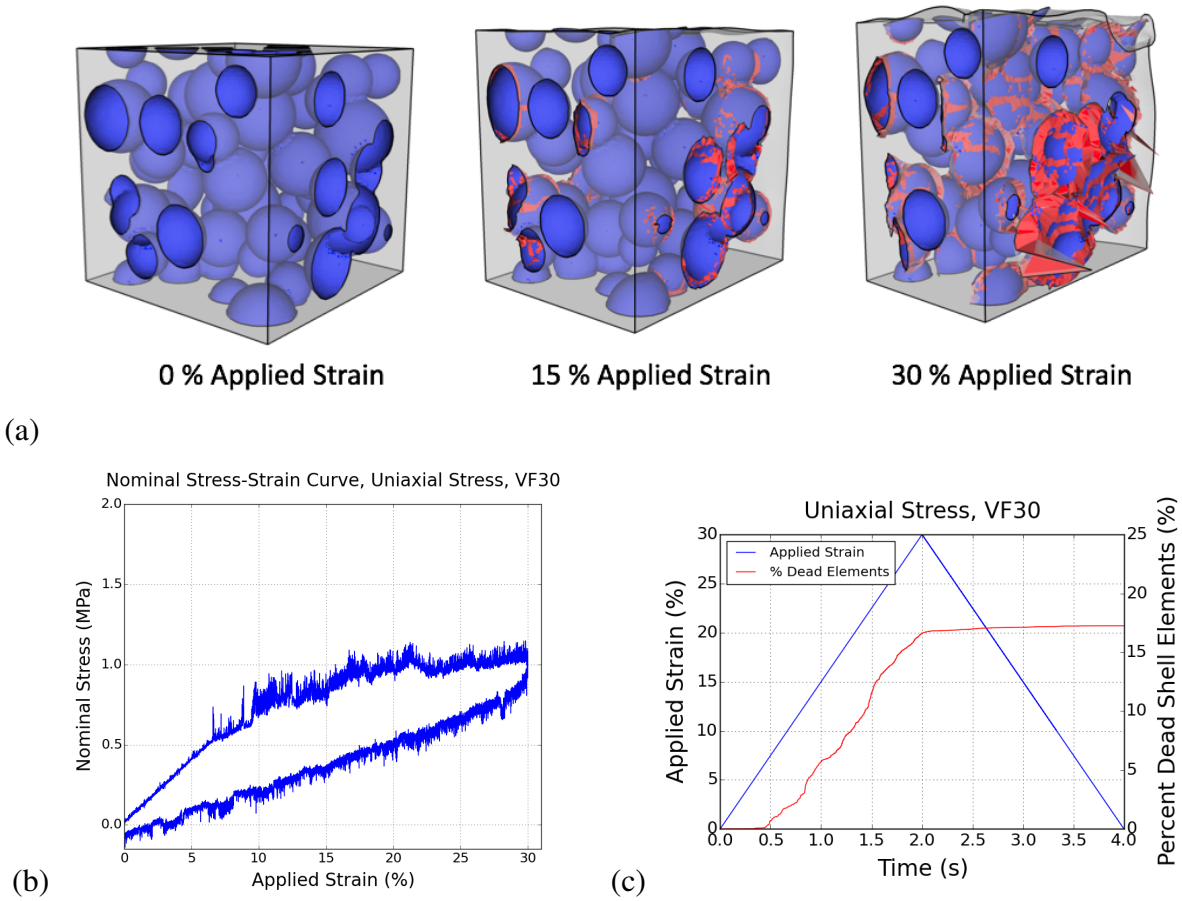


**Figure 10.** Sylgard/GMB with 30% volume fraction GMBs under unaixial stress BVP: (a) Deformation sequence with dead shell elements shown in red, (b) Nominal stress-strain curve, (c) Accumulated number of dead shell elements vs. time.

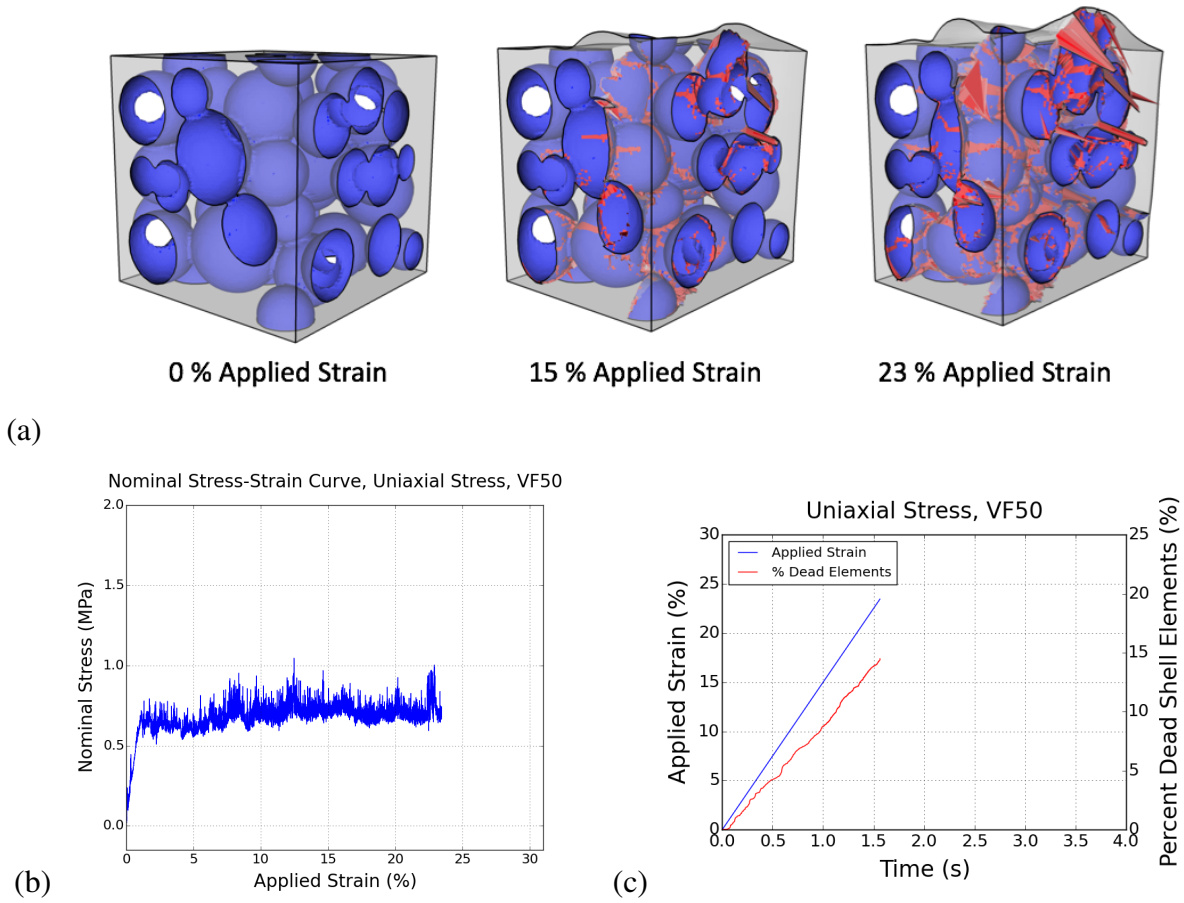


**Figure 11.** Sylgard/GMB with 50% volume fraction GMBs under unaixial stress BVP: (a) Deformation sequence with dead shell elements shown in red, (b) Nominal stress-strain curve, (c) Accumulated number of dead shell elements vs. time.

### 2.5 Predictions of Behavior in Uniaxial Strain Boundary Value Problem (confined compression)

Figure 12(a) shows the nominal stress-strain response of Sylgard/GMB materials with various GMB volume fractions in the uniaxial strain BVP. Again, the response of pure Sylgard (dark blue line) is included for comparison. The cumulative percentage of dead shell elements for each Sylgard/GMB material is shown in Figure 12(b) and Table 2.5 contains the same metrics of initial and unload slopes, etc as considered in the uniaxial stress case. It should be noted that the uniaxial

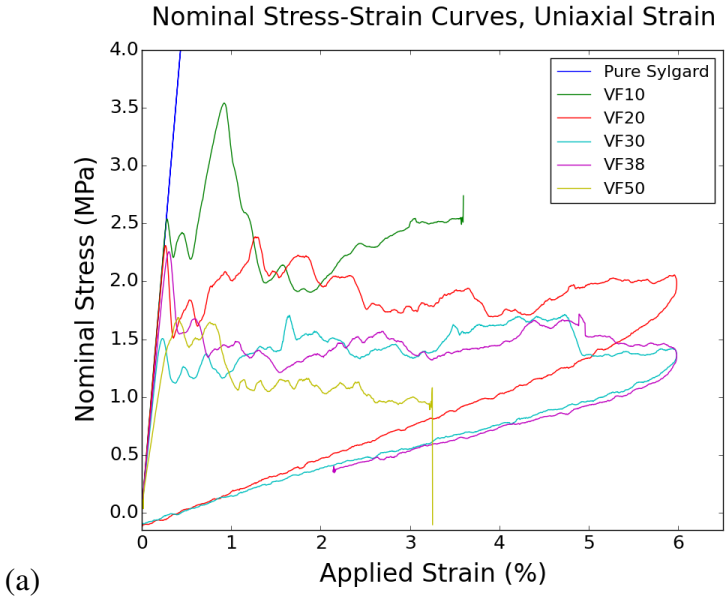


(a)

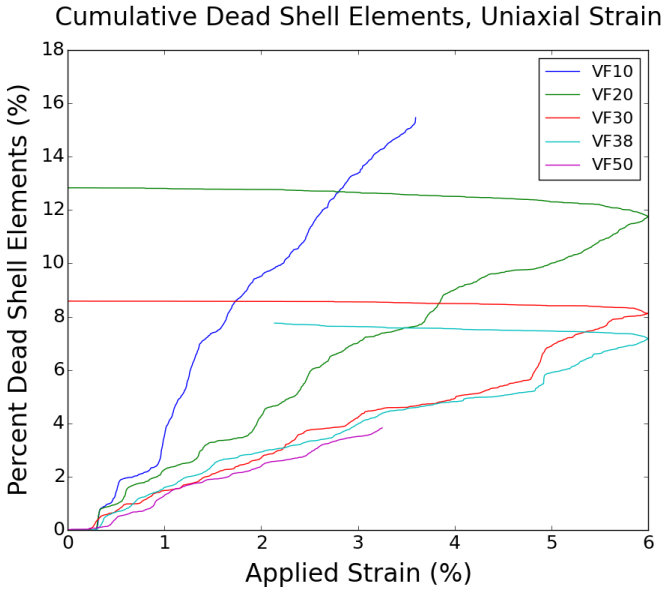


(b)

**Figure 12.** Stress-strain curves (a) and accumulated number of dead shell elements (b) for Sylgard/GMB materials with various volume fractions under the unaixial strain BVP.

**Table 3.** Summary of Load/Unload Slopes, Plateau Stress Behavior, and Strain at Initial GMB Breakage for various GMB volume fractions under uniaxial strain BVP (confined).

| **GMB Volume Fraction** | **Initial Loading Slope (MPa)** | **Unload Slope (MPa)** | **Plateau Stress (MPa)** | **Strain at Initial GMB Breakage** |
|---|---|---|---|---|
| Pure Sylgard | 905.7 | 905.7 | – | N/A |
| 10% | 933.5 | ** | ∼2.4 | 0.294% |
| 20% | 912.4 | 25.5 | ∼1.9 | 0.283% |
| 30% | 770.3 | 17.5 | ∼1.4 | 0.202% |
| 38% | 832.4 | 17.0 | ∼1.4 | 0.251% |
| 50% | 571.8 | ** | ∼1.0 | 2.5e-7% |

** Simulation failed before unload, – No plateau behavior observed

strain simulations were much less computationally robust compared to the unaixal stress, and several of them failed before reaching the maximum prescribed strain of 6%. However, we can still observe many features of the response for comparison between different GMB volume fractions.

In this uniaxial strain boundary value problem, plateau stress behavior is seen for all GMB volume fractions, the magnitude of which decreases with increasing volume fraction. Additionally, the GMBs start to break at roughly the same strain of ∼0.2% in all cases. The key feature seen in Figure 12(b) is that the initiation of damage is independent of GMB volume fraction under uniaxial strain conditions. This indicates that the mode of GMB damage accumulation is fundamentally different between the uniaxial strain and uniaxial stress boundary value problems.

Again, pure Sylgard does not have this plateau behavior, as no damage mechanisms are available in the pure material. In the case of confined uniaxial-strain compression, the effects of this are much greater than when under unconfined unaixial stress as the bulk modulus of pure Sylgard is high (920 MPa). Thus, the pure Sylgard exhibits much greater stresses even at small strains than the materials containing any volume fraction of GMBs (Figure 12(a)).

The initial loading slopes are used to evaluate the uniaxial strain modulus, which is closely related to the bulk modulus. For low GMB volume fractions 10% and 20%, the loading slopes are slightly higher than that of pure Sylgard. This follows the predictions from composite theory in Section 1 that the bulk modulus should increase with increasing GMB volume fraction. However, at GMB volume fractions of 30% and above, the initial slope decreases substantially, which is the opposite trend from that predicted in Section 1. We hypothesize this is due to differences in the FE model from the assumption of uniform sized spherical particles used in the composite theory, such as allowing GMBs to overlap each other, intersect the SVE faces, and the Gaussian distribution of GMB radii. Additionally, volume fractions higher than 20% are likely above the dilute limit for which the composite theory is accurate. Further study would be necessary to test these hypotheses and better understand the relationship between the bulk modulus and GMB volume fraction.

Figures 13, 14, and 15 show snapshots of the modeled microstructures correlated with the individual stress-strain response and damage evolution for GMB volume fractions of 10%, 30%, and 50%, respectively. These microstructure snapshots are shown at 1%, and 3% strain since all simulations ran successfully up to this strain. For the 10% GMB volume fraction (Figure 13), the failure mode of individual GMBs appears to be widespread death of most elements in a particular GMB. This complete failure of individual GMBs correlates to the jagged nature of the plateau region in the nominal stress-strain curve, where sharp drops in stress occur when a GMB fails and the material rapidly loses stiffness in that local region. This is different than the uniaxial stress case, where individual GMBs showed discrete regions of dead elements with other regions of the GMB still intact and the plateau region of the nominal-stress strain curves did not exhibit large stress variations. At the higher volume fractions of 30% - 50% (Figures 14 - 15), the GMB damage looks more similar to the uniaxial stress cases with more discrete regions of dead elements. This correlates with the trend shown in Figure 12(b), where the two lower volume fractions of 10% and 20% accumulate a higher percentage of dead shell elements than the higher volume fractions 30% - 50%. More thorough study through both experimental and modeling efforts would be needed to validate and explain these differences in GMB failure mode.

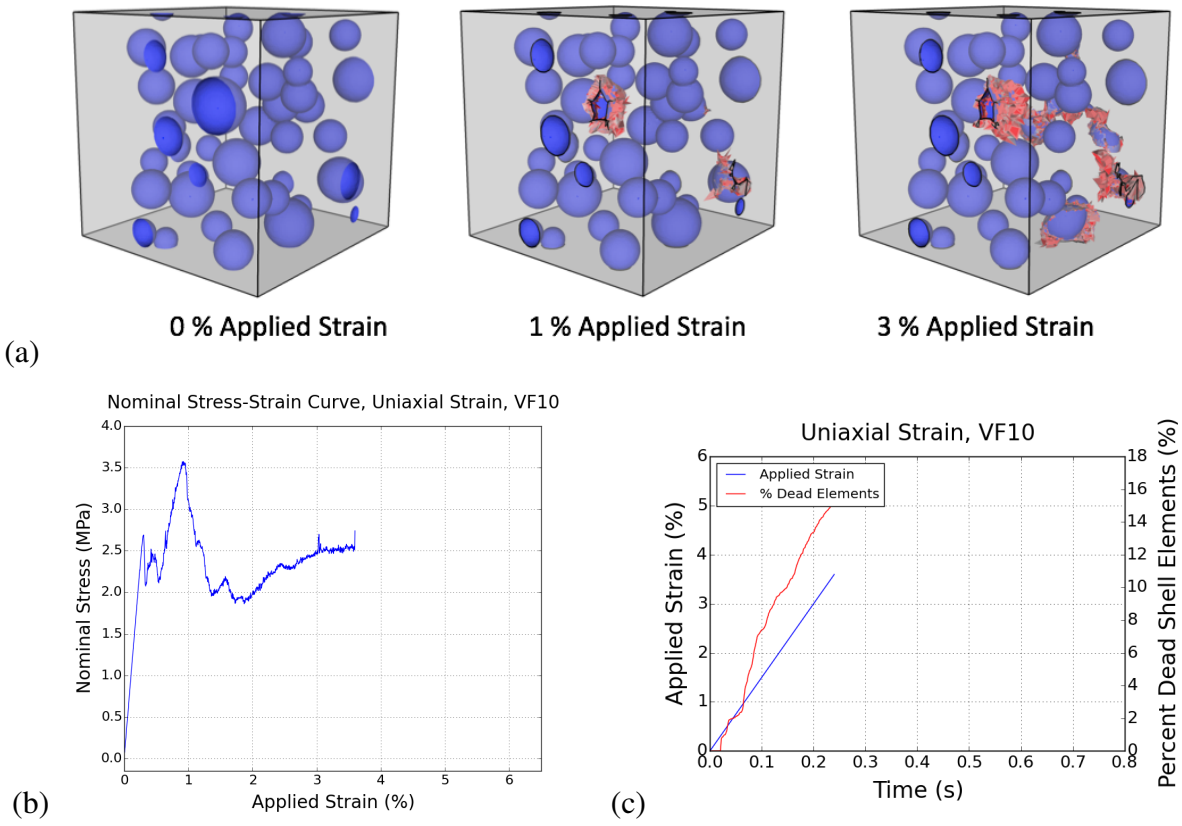


**Figure 13.** Sylgard/GMB with 10% volume fraction GMBs under unaixial strain BVP: (a) Deformation sequence with dead shell elements shown in red, (b) Nominal stress-strain curve, (c) Accumulated number of dead shell elements vs. time.

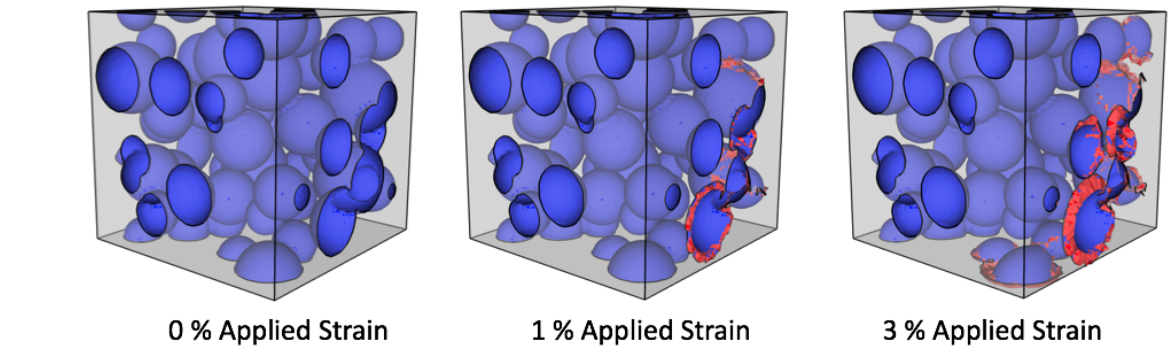


(a)

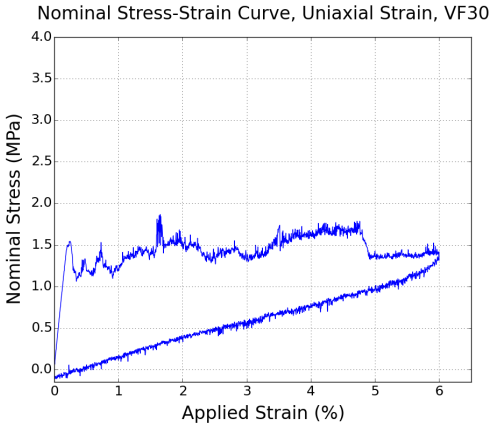


(b)

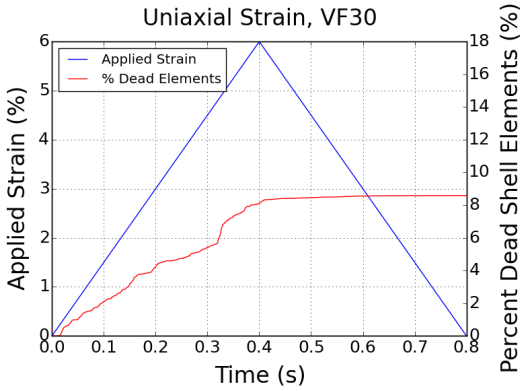


(c)

**Figure 14.** Sylgard/GMB with 30% volume fraction GMBs under unaixial strain BVP: (a) Deformation sequence with dead shell elements shown in red, (b) Nominal stress-strain curve, (c) Accumulated number of dead shell elements vs. time.

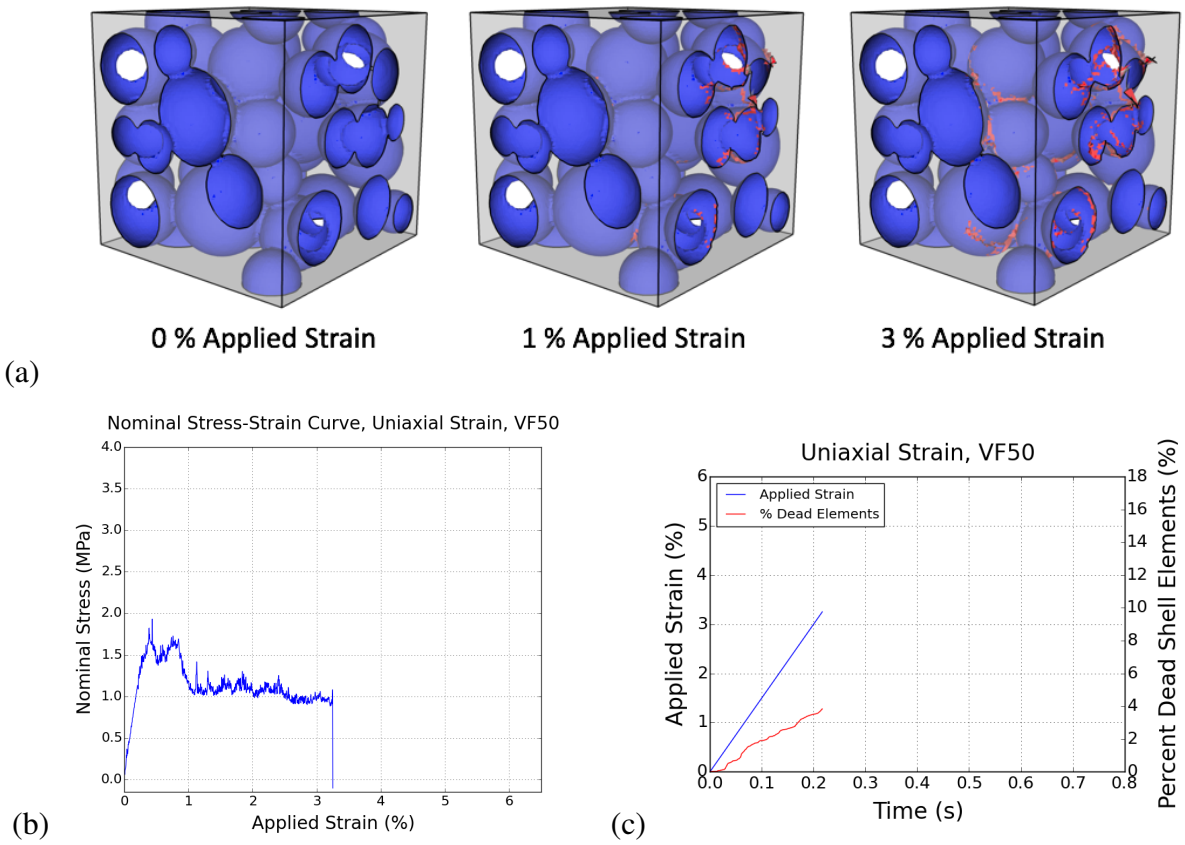


**Figure 15.** Sylgard/GMB with 50% volume fraction GMBs under unaixial strain BVP: (a) Deformation sequence with dead shell elements shown in red, (b) Nominal stress-strain curve, (c) Accumulated number of dead shell elements vs. time.

### 2.6 Caveats to FE Results

There are a few key caveats to consider when evaluating the above Finite Element results.

- The effects of several geometric features of the SVE models that were necessary to generate high GMB volume fractions above 30% are unknown, and it is still undetermined as to how the following features change the physical representativeness of the model.
  - Allowing GMBs to intersect each other. This may introduce non-physical structures like multiple intersecting GMBs that create hollow pathways through the material, particularly in the models with high GMB volume fractions.
  - Allowing GMBs to intersect the SVE faces. Without periodic boundary conditions, this introduces partial GMB structures on the edges that will behave differently than the intact spherical GMBs. We are unsure how much this affects the global material response, but we anticipate it will be softer than a periodically constrained surface since the partial GMBs on the boundary act like damaged structures (compared to the whole GMBs) in our current approach.
- Only one realization of the microstructure at each GMB volume fraction was studied. Stronger conclusions could be drawn if multiple realizations were studied. This would allow the effects of variability in GMB arrangement, etc to be considered.
- Our failure stress for GMBs is estimated, and thus the above results should be considered qualitatively and in light of identifying relative trends between different GMB volume fractions. Quantitate features, such as the exact volume fraction necessary to achieve a particular behavior, may change if a different failure stress was used.

## 3 Conclusions and Key Findings

Both analytic composite theory and finite element simulations of explicitly resolved material constituents at the meso-scale subjected to large compressive strains have been used to study the effect of GMB volume fraction on the behavior of Sylgard/GMB composites. Key findings are summarized below:

- The composite theory is most valid at low GMB volume fractions, and predicts that with increasing GMB volume fraction, shear and bulk modulus will increase while the coefficient of thermal expansion will decrease.
- Finite element simulations showed a mechanism where breakage of individual GMBs limited the maximum stress reached in the material, and higher GMB volume fractions resulted in lower maximum global stresses. This was seen in both uniaxial stress and uniaxial strain boundary value problems, but with some differences summarized here.

  - The uniaxial stress responses showed clear differences in behavior with increasing GMB volume fraction. At low GMB volume fractions, GMB breakage did not occur until large strains and the stress-strain response was similar to that of pure Sylgard. At higher GMB volume fractions, GMB breakage started much sooner and resulted in a stress-limiting plateau behavior.
  - The unaixial strain responses showed a stress-limiting plateau at all GMB volume fractions, and GMB breakage occurred at roughly the same low strain for all cases. In this boundary value problem, none of the Sylgard/GMB materials resembled the response of pure Sylgard which reached much higher stresses.

- The composite theory showed reasonable agreement at low GMB volume fractions when comparing elastic moduli with initial loading slopes in the finite element studies. At higher volume fractions, the bulk moduli did not agree between methods. This suggests that the bulk modulus has a potentially complex relation with volume fraction that would benefit from further study.

## References

[1] R. M. Christensen. *Mechanics of Composite Materials*. Dover Publications, Inc., Mineola, New York, 2nd edition, 2005.

[2] K.N. Long. Elastic constants of sylgard 184 filled with 3m a16/500 glass microballoons (sand2016-2349 uur). MEMO (UUR) SAND2016-2349 UUR, Sandia National Laboratories, March 2016.

[3] K. N. Long, J. Carroll, J. A. Brown, M. E. Stavig, and K. R. Ford. Preliminary investigation and modeling of the mechanical behavior of sylgard 184 impregnated with a16/500 glass micro-balloons. SAND Report OUO 2015-10847, Sandia National Laboratories, December 2015.

[4] Sandia National Laboratories Douglass B. Adolf. Polymer properties database. http://www.sandia.gov/polymer-properties/classes_of_polymers.html, September 2014.

[5] X. Nie and W.W. Chen. *Journal of the American Ceramic Society*, 90(8):2556–2562, 2007.

[6] S. Chocron, K.A. Dannemann, J.D. Walker, A.E. Nicholls, and Jr. C.E. Anderson. *Journal of the American Ceramic Society*, 90(8):2549–2555, 2007.

[7] I. D. Johnston, D. K. McCluskey, C. K. L. Tan, and M. C Tracey. Mechanical characterization of bulk sylgard 184 for microfluidics and microengineering. *Journal of Micromechanics and Microengineering*, 24, January 2014.

[8] Z. H. Karadeniz and D. Kumlutas. A numerical study on the coefficients of thermal expansion of fiber reinforced composite materials. *Composite Structures*, 78:1–10, 2007.

[9] S.J. Owen, M.L. Staten, and M.C. Sorensen. Parallel hex meshing from volume fractions. In *Proceedings 20th International Meshing Roundtable*, pages 161–178, 2011.

[10] Mathew Lewis, Rebecca Cohenour, and Tom Stephens. Viscoelastic properties of three sylgard 184 formulations from torsional dynamic modulus testing. LA-UR 07-0298, Los Alamos National Laboratory, June 2007.

[11] K.N. Long and J.A. Brown. A linear viscoelastic model calibration of sylgard 184. Memo (uur), Sandia National Laboratories, April 2017.

[12] SIERRA Solid Mechanics Team. *Sierra/SolidMechanics 4.42 User's Guide*. Computational Solid Mechanics and Structural Dynamics Department Engineering Sciences Center Sandia National Laboratories, Box 5800 Albuquerque, NM 87185-0380, 4.42 edition, October 2016.